Hierarchical clustering of spectral images with spatial constraints for the rapid processing of large and heterogeneous datasets

Gilles Celeux, Serge X. Cohen, Agnès Grimaud, Pierre Gueriau

HAL Id: hal-03104488
https://hal.uvsq.fr/hal-03104488v2

Preprint submitted on 11 Jul 2021 (v2), last revised 10 Apr 2022 (v4)

Hierarchical clustering of spectral images with spatial constraints for the rapid processing of large and heterogeneous datasets

Gilles Celeux[*], Serge X. Cohen[†], Agnès Grimaud[‡], and Pierre Gueriau[§]

Abstract.

When dealing with full spectrum images in which each pixel is characterized by a full spectrum, ie. spectral images, standard segmentation methods, such as k-means or hierarchical clustering might be either inapplicable or inappropriate ; one aspect being the multi-GB size of such dataset leading to very expensive computations. In the present contribution, we propose an approach to spectral image segmentation combining hierarchical clustering and spatial constraints. On the one hand spatial constraints allow to implement an algorithm with a reasonable computation time to obtain a segmentation and with a certain level of robustness with respect to the signal-to-noise ratio since the prior knowledge injected by the spatial constraint partially compensates for the increase in noise level. On the other hand hierarchical clustering provides a statistically sound and known framework that allows accurate reporting of the instrument noise model. In terms of applications, this segmentation problem is encountered particularly in the study of ancient materials that benefits from the wealth of information provided by the acquisition of spectral images. In the last few years, data collection has been considerably accelerated, enabling the characterization of the sample with a high dynamic range in both the spatial dimensions and composition and leading to an average size of a single dataset in the tens of GB range. Hence we also considered computational and memory complexity when developing the herein proposed algorithm. Taking on this application domain, we illustrate the proposed algorithm on a X-ray fluorescence spectral image collected on an ca. 100 Myr fossil fish, as well as on simulated data to assess the sensitivity of the results to the noise level. For such experiment, the lower sensitivity to noise simultaneously lead to an increase in the spatial definition of the collected spectral image, thanks to the faster acquisition time, and to a reduction in the potentially harmful radiation dose density to which the samples are subjected.

Key words. Spectral image segmentation, Ward criterion, spatial constraint, ancient material, X-ray fluorescence

1. Introduction

Spectral imaging, ie. the collection of images for which each pixel is characterized by a full spectrum (see eg. Fig. 1), is a tool of choice for simultaneously obtaining physico-chemical information (eg. elemental, chemical or mineralogical composition), and the morphological information essential for describing heterogeneous materials. Spectral images are particularly used to study ancient materials, such as encountered in archaeology and paleontology or as

[*]Inria Saclay-Île-de-France, IMO campus d'Orsay 91405 Orsay.

[†]IPANEMA, CNRS, ministère de la Culture, UVSQ, MNHN, USR3461, Université Paris-Saclay, 91192 Gif-sur-Yvette, France (serge.cohen@ipanema-remote.fr).

[‡]Université Paris-Saclay, UVSQ, CNRS, Laboratoire de Mathématiques de Versailles, 78000 Versailles, France.

[§]Institute of Earth Sciences, University of Lausanne, Géopolis, CH-1015 Lausanne, Switzerland.

part of the cultural heritage research, which are very diverse but share the particularity of being composite and heterogeneous on several scales [6]. They are also the results of multiple processes at various time scales, inducing strong constraints in terms of handling and physico-chemical characterization whilst often having limited a priori certainties concerning them [5, 4, 7], making spectral imaging a unique approach to collect information on past states recorded in the materiality of these objects, and to understand their alteration through time.
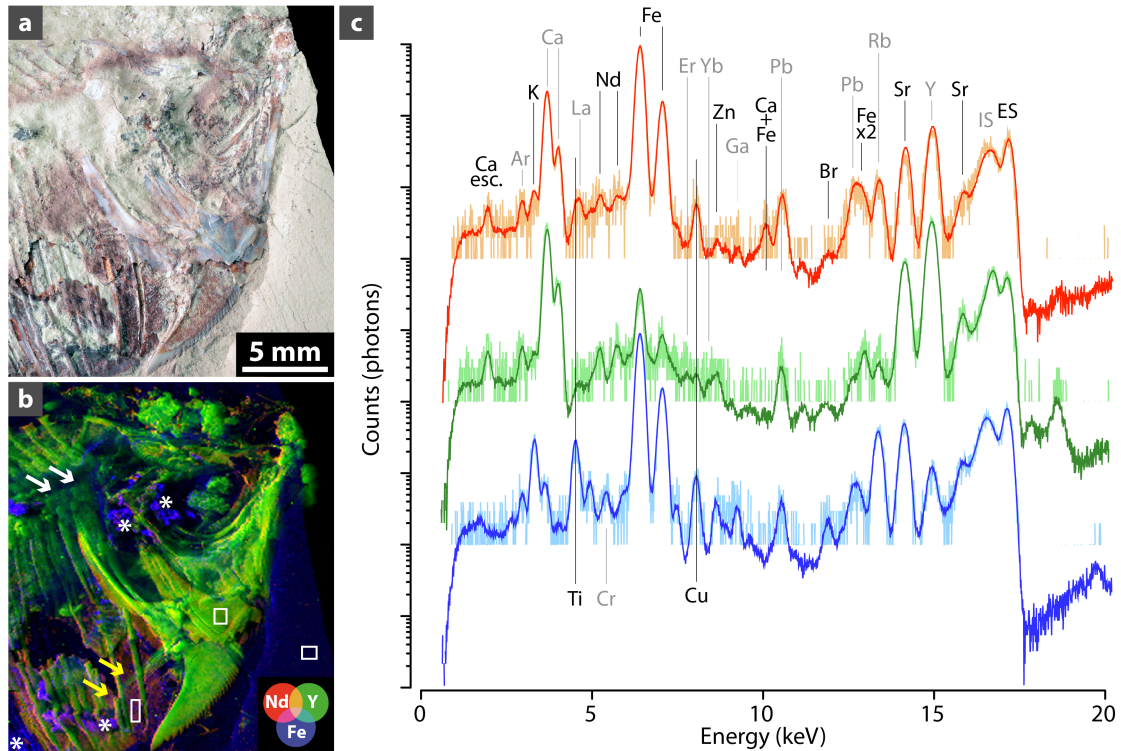
Figure 1. Synchrotron XRF mapping of major-to-trace elements of the anterior part (skull on the right) of the yet undescribed fish MHNM-KK-OT 03a from the Jbel Oum Tkout Lagerstätte (Upper Cretaceous, 100 Myr, Morocco). (a): optical photograph. (b): false color overlay of the distributions of two rare earth elements, neodymium (red) and yttrium (green), and of iron (blue), reconstructed from a full spectral decomposition of the data (modified from [16]). Acquisition parameters: 100 x 100 μm^2 scan step, 50,851 pixels. Lighter tones indicate higher concentrations. Arrows and asterisks in b are discussed in the text. (c): Mean (dark colored; 90 pixels) and central individual (light colored) spectra from the boxes in b, corresponding to fossilized muscles (red and orange), bone (dark and light green) and the sedimentray matrix (dark and light blue), respectively. Spectra are shown using a logarythmic scale, vertically shifted for clarity. Main peaks are labelled. Abbreviations: esc., escape peak; ES, elastic scattering; IS, inelastic scattering; x2, sum (double) peak. Note that the Ar-peak does not arise from the sample but is due to excitation of Ar in the air (ca. 0.93 %) between the sample and the detector.

Spectral imaging datasets make several GB or even tens of GB, depending on the type of detection used. Indeed, while 1D detectors typically record thousands of values (ie. a few KB) per pixel, 2D array detectors record images of several MB per pixel (eg. [1, 3, 17]). As such,

2

these datasets are too massive to be timely exploited with standard algorithms and we need to develop algorithms able to analyze such images and if possible in a timeframe compatible with the data collection time to provide feedback possibilities on the measurements (eg. [1, 3]). To our knowledge, no existing method tackles this very problem. One should also consider that on those measurements involving a probe, increasing the signal to noise ratio (SNR) comes at a cost: increasing probe/material interaction indeed most often leads to longer measurement times and always to a higher radiation dose deposited in the material. In such a framework one has to find a balance between SNR and dose/time, so that the experiment is conclusive without producing alteration of the samples during the analysis (eg. [15]).

In this article, we focus on the question of image segmentation when the dataset comes from X-ray fluorescence (XRF) mapping, a technique by which each individual pixel is characterized by its XRF spectrum, providing elemental composition information on that pixel (Fig. 1). The classical approach to plot quickly or even live elemental distributions recorded by XRF mapping consists of integrating the signal (ie. photons counted by the detector) in spectral regions of interest (ROI) corresponding to targeted element peaks. This does not, however, hold true elemental distribution images as such ROI integrations additionally include significant contributions from other elements or phenomena (namely scattering, and sum and escape peaks); these overlapping biases can only be circumvented by applying slower approaches allowing a spectral decomposition of the dataset (eg. [16, 1]). Furthermore, while providing dimensional reduction, such processing does not provide a segmentation of the material and could only be an intermediate step towards the identification of specific constituent of the material and their morphological features. An efficient model when it comes to analyse this type of samples is to consider that an image is made of a set of patches of uniform composition taken from a small, but unknown, set of compositions. This leads to two determining parameters for the model, the number of present compositions, ie. the number of classes in the segmentation, and the mean size of the patches which can also be measured as the patch density, that is the number of patches per unit surface of the image.

In the following, in Sect. 2, we propose a hierarchical segmentation algorithm combining the characteristics of hierarchical clustering with the imaging properties of a composite material. Compared to other methods, such k-means, agglomerative clustering provides a natural entry to apply spatial constraints. Furthermore, in the targeted imaging applications, the number of classes (K) is not known a priori, and hierarchical clustering provides a structured way for the application domain scientist to assess the likely value(s) of K. In other words, we aim at proposing a hierarchical classification procedure with spectral dissimilarities allowing to take into account the spatial proximities between the pixels. Furthermore, the proposed

This manuscript is currently submitted to peer-review.

method is able to estimate the patch density when it is not known a priori.

It is important to understand the nature of the signal measured in such experiment. In XRF, we measure the energy of the photons emitted by the material when it is subjected to monochromatic incident radiation. Because this re-emission phenomenon is a stochastic process, the measured spectrum is an empirical sampling of the law of this process. Instead of analyzing the signal using generic tools for Euclidean spaces, such as the ℓ_2 distance, it is therefore more relevant to use tools adapted to the comparison of population samples. On this respect, the algorithm we propose is based on the χ^2 as a tool to assess homogeneity between two samples, in the present case two pixels for which we want to test the potential similarity in composition.

After defining the terms and notations used throughout this article, we expose the general framework of our dissimilarity measure (using a Ward criteria based on χ^2, Sect. 2.2), and then propose an approach to impose spatial constraint upon the agglomerative process of the hierarchical clustering in Sect. 2.3, effectively segmenting the image into patches. Then, in Sect. 3, we concentrate on the proper steps at which the spatial constraint should be released to properly account for non connex domains made of the same material. We further consider the appropriate number of classes at which the agglomeration process should be stopped in Sect. 4. To illustrate our approach, we apply the proposed algorithm on a true dataset corresponding to the XRF mapping of a fossil teleost fish, including both the analysis of the experimental dataset in Sect. 5, and, in Sect. 6, the analysis of a synthetic dataset resembling the experimental one but providing the possibility to simulate various signal to noise ratio and giving insight into the robustness of the proposed algorithm to the noise level.

2. The proposed hierarchical clustering method

2.1. Notations and definitions

A spectral image of N pixels is considered. And each pixel $i \in \{1, ..., N\}$ is characterized by a spectrum $\mathcal{S}_i = (s_i(p))_{p \in \{1, ..., P\}}$, where $s_i(p)$ is the number of photon counts for pixel i in energy canal p.

For $i \in \{1, ..., N\}$ and $p \in \{1, ..., P\}$, let

$$f_{i,p} = \frac{s_i(p)}{s_{\bullet\bullet}} \text{ and } t_p^i = \frac{s_i(p)}{s_{i\bullet}} \text{ where } s_{i\bullet} = \sum_{p=1}^{P} s_i(p) \text{ and } s_{\bullet\bullet} = \sum_{i=1}^{N} s_{i\bullet}.$$

The aim is to propose a hierarchical classification procedure of spectra $(\mathcal{S}_i)_{i \in \{1, ..., N\}}$ using the conditional distributions (or profiles) of pixels $((t_p^i)_{p \in \{1, ..., P\}, i \in \{1, ..., N\}})$, the pixel i being weighted by $f_{i\bullet} = s_{i\bullet}/s_{\bullet\bullet}$ ($i \in \{1, ..., N\}$).

Since these profiles are probability distributions and the aim is to assess homogeneity

4

between two pixels from their spectra (i.e. their potential similarity in composition), the comparaison of two profiles is made using the χ^2 euclidean distance.

So for two pixels i and j, let

$$d_{\chi^2}^2(\mathcal{S}_i, \mathcal{S}_j) = \sum_{p=1}^{P} \frac{(t_p^i - t_p^j)^2}{f_{\cdot p}}$$

with $f_{\cdot p} = \sum_{i=1}^{N} f_{i,p} = \frac{1}{s_{\cdot\cdot}} \sum_{i=1}^{N} s_i(p)$.

Remarks:

- It is assumed that $f_{\cdot p} \neq 0$ for all p. If there is a canal p such that $f_{\cdot p} = 0$, then $s_i(p) = 0$ for all $i \in \{1, ..., N\}$, hence $t_p^i = t_p^j = 0$ for all $(i, j) \in \{1, ..., N\}^2$. Thus, such canals are removed beforehand.
- It is assumed that $s_{i\cdot} \neq 0$ for all pixel i (otherwise it would mean that the detector did not received any photon for the corresponding pixel).

2.2. The Ward criterion

Using the χ^2 euclidean distance as the proximity measure between the spectra of pixels, the hierarchical clustering is designed with the agglomerative Ward criterion δ_{χ^2} [23], which consists of minimizing the increase of the within-cluster inertia at each step. This agglomerative criterion for two clusters C and C' is:

$$(2.1) \qquad \delta_{\chi^2}(C, C') = \frac{\mu_C \mu_{C'}}{\mu_C + \mu_{C'}} d_{\chi^2}^2(S_{g_C}, S_{g_{C'}})$$

where $\mu_C = \sum_{i \in C} f_{i\cdot}$ is the weight of cluster C and S_{g_C} the gravity center of cluster C;

$S_{g_C} = (g_c(p))_{p \in \{1, ..., P\}}$ with $g_c(p) = \frac{1}{\mu_C} \sum_{i \in C} f_{i\cdot} t_p^i$.

Note that the gravity center of the union of two clusters is $S_{g_{C \cup C'}} = \frac{\mu_C S_{g_C} + \mu_{C'} S_{g_{C'}}}{\mu_C + \mu_{C'}}$.

Usually, the dissimilarity matrix between clusters is updated with a specific occurrence of the general Lance and Williams formula, see [12, 18] for example. The dissimilarity between the possible aggregation $C_i \cup C_j$ of two clusters C_i and C_j and any other cluster C_k can be expressed by:
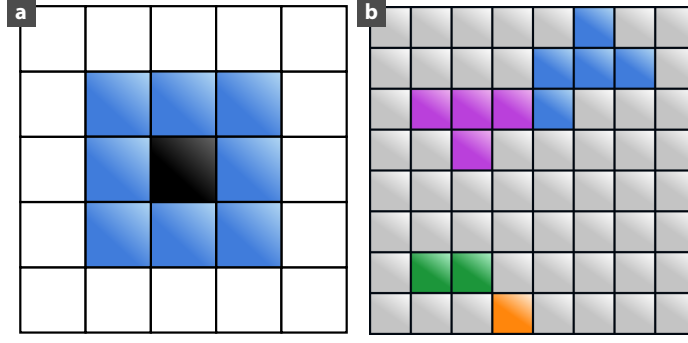
5

Figure 2. Schematic representation of the second-order neighborhoods approach. (a): neighbors for a pixel that is not located on an edge or at a corner. (b): example of clusters spatially neighboring; on the top, the blue and purple clusters are spatially neighboring, while on the bottom left the green and orange clusters are spatially neighboring. All are spatially neighboring to the grey cluster. On another hand, for example, the purple and orange clusters are not spatially neighboring.

$$\delta_{\chi^2}(C_k, C_i \cup C_j) = \frac{1}{\mu_{C_i} + \mu_{C_j} + \mu_{C_k}} \times$$

(2.2)

$$\left((\mu_{C_k} + \mu_{C_i})\delta_{\chi^2}(C_k, C_i)\right.$$
$$+ (\mu_{C_k} + \mu_{C_j})\delta_{\chi^2}(C_k, C_j)$$
$$\left. - \mu_{C_k}\delta_{\chi^2}(C_i, C_j)\right)$$

2.3. Taking the spatial constraint into account

With spectral images, the dimension of the dissimilarity matrix at the start is too large ($\mathcal{O}(N^2) \approx 20$ GB) and it is computationally too expensive ($\mathcal{O}(N^2 P) \approx 5 \times 10^{12}$ operations to design directly a hierarchical clustering with the Ward criterion described above). Moreover, as mentioned in the introduction, an image is made of a set of patches of uniform composition. Hence it is desirable that the clusters form unions of patches, that is spatially connected sub-clusters.

For these two reasons, following [19], we propose a first hierarchical clustering algorithm that only aggregates two spatially neighboring clusters. More precisely, two clusters C and C' are spatially neighboring if there exists $(i, i') \in C \times C'$ such that i and i' are neighboring pixels.

In our application, we will consider second-order neighborhoods (Fig. 2). It implies that most of the pixels have eight neighbors (Fig. 2a), while the pixels on an edge or at the corners have only five and three neighbors, respectively.

The advantage of this algorithm is, at each step, that for each cluster only a few dissimi-

6

larities have to be computed. Nevertheless, for this reason, it is not possible to use the Lance and Williams formula [12, 18] to update the dissimilarities. Therefore, equation 2.1 is used to compute the dissimilarities needed to design the hierachy.

The hierarchical algorithm with the spatial constraint operates following the steps below:

Algorithm 2.1 Hierarchical spatial clustering

   Initialization : computes the χ^2 distances between two spectra for neighboring pixels
   Define $L := 1$
   while $L < N$ do
      Aggregates the two neighboring clusters with the smallest Ward criterion value (or χ^2 distances at the first step)
      Updates the neighborhoods of clusters.
      Updates the dissimilarity matrix (for spatially neighboring clusters).
      $L := L + 1$
   end while

If this algorithm is run until it remains only two clusters, we get a hierarchy where at each step the clusters are spatially connected. However, it is not desirable to impose such clusters connexion during the final steps. Indeed, from the point of view of the application domain scientist/specialist, the relevant clusters, while connected at fine scale, have no reason to be spatially connected at large scale. For example, when imaging a fossil, several bones will have a similar composition without touching each other.

As a consequence, the proposed algorithm taking the spatial constraint into account is run for J steps leading to spatially connected clusters, J being large (the choice of the switching step J will be discussed hereafter in Sect. 3). It leads to $(N - J)$ spatially connected clusters or patches as called before. Then from these $(N - J)$ patches, unconstrained agglomerative hierarchical clustering algorithm with the Ward criterion is used. Thus, the proposed final clusters are union of the $(N - J)$ patches. Obviously, a relevant number of final clusters is to be chosen; this point is discussed in Sect. 4.

3. Selecting the switching step J

In the following, the patch density (for a unit surface of one pixel) is noted $\delta_p(\in]0, 1[)$. When the patch density of the sample is known a priori, the switching step is set so that the number of patches is an integer close to $\delta_p \times N$. This leads to release the spatial constraint at the step being the closest integer to $(1 - \delta_p) \times N$. Still, in most cases, the patch density is unknown and we herein propose a method to estimate this morphological characteristic of the sample and to select J.

3.1. The proposed criterion

In order to select the switching step J in the proposed hierarchical algorithm, a criterion balancing the between-cluster inertia with a regularization term measuring the spatial homogeneity of the clusters is proposed. This criterion to be maximized has the form:

$$H(J) = B(J) + \alpha G(J),$$

where $\alpha \in \mathbb{R}_+$, $B(J)$ is the between-cluster inertia of a partition of the pixels into $(N - J)$ patches and $G(J)$ is a measure of the spatial homogeneity of this partition. Following [2], we consider

$$G(J) = \frac{1}{2} \sum_{k=1}^{J} \sum_{i=1}^{N} \sum_{j=1}^{N} c_{ik} c_{jk} v_{ij}$$

where $v_{ij} = 1$ if i and j are neighbors, and 0 otherwise (with $v_{ii} = 0$ by convention), and $c_{ik} = 1$ if $i \in C_k$ and 0 otherwise.

To weight the $B(J)$ and $G(J)$ terms of the criterion, we can choose the scalar α to get a perfect balance between the two extreme cases : N clusters (ie. a nul intra-cluster inertia) and one cluster (ie. a perfect spatial homogeneity).

In the extreme situation of a partition into N clusters, we have $G(N) = 0$ and in the opposite extreme situation $G(1) = \frac{1}{2} \sum_{i=1}^{N} \sum_{j=1}^{N} v_{ij} \approx \frac{1}{2} \sum_{j=1}^{N} 8 = 4N$. (For simplicity, we consider here improperly that each pixel has 8 neighbors.)

Assuming a balance between these two extreme situations $H(N) = H(1)$ leads to $\alpha = \dfrac{T}{4N}$, with $T = B(N)$ being the total inertia of the whole set of pixels. Thus, the criterion to be maximized is

$$H(J) = B(J) + \frac{T}{4N} G(J).$$

However, as it will be apparent in the case study in Sect. 5, the choice of this criterion leads to the selection of a too large number of agglomerative steps $J_{\max}$, in other words of $(N - J_{\max})$ patches that are too small.

8

In order to select a more relevant number of patches, from which to release spatial constraints in the clustering, we propose to make use of the "one standard deviation" procedure proposed in [8] to cut a decision tree. This procedure consists of computing $H(K)$ for $K = N, \ldots, 1$, then to compute the standard error $\mathrm{sd}(H)$ of the resulting $(H(K))_{K=N,\ldots,1}$ and choosing the smallest $\hat{J}$ such that

$$H(\hat{J}) \geq H(J_{\max}) - \mathrm{sd}(H).$$

The rationale for this procedure is to determine the value of $\hat{J}$ that corresponds to a balanced number of patches that provides a good compromise between the between-cluster inertia and the spatial homogeneity. Note that, while it is expected that $H(J)$ increases from $H(N)$ to $H(J_{\max})$ and then decreasing back to $H(1)$, there is no guarantee for such a behaviour. Such an unexpected behaviour of the H criterion is obtained in particular for low signal to noise ratio image in Fig. 6e and g. In order to also address these types of behaviour of H we express the choice of $\hat{J}$ in a different way :

$$\hat{J} = \max\{J|(J \leq J_{\max}) \text{ and } (H(J) \leq H(J_{\max}) - \mathrm{sd}(H))\}$$

And this leads to estimate the patch density δ_p by $\hat{\delta}_p = \dfrac{N - \hat{J}}{N}$.

3.2. Heuristic to obtain $\hat{J}$ in practice

In practice, depending on the image size, it can be too long to compute $H(K)$ for all $K \in \{N, \ldots, 1\}$. In this case, the following heuristic approach is proposed to determine $\hat{J}$ using the patch density:

As a first step, the idea is to compute $(H(\ell \times by))_l$, with $by \geq 1$ chosen to have a reasonable computing time and $\ell \in \mathbb{N}^*$ such that $\ell \times by \leq N$. However, after testing on the studied dataset described in Sect. 5, we noticed that the obtained $\hat{J}$ can change significantly according to the value by. Hence, by must be small enough to obtain a correct value for $\hat{J}$ (but we do not know its order of magnitude).

On the other hand, as seen above, the proper switching step $\hat{J}$ and the proposed estimation of the patch density δ_p are related. Therefore, in this case, we first propose to evaluate the "constant" δ_p, which is linked to the morphology of the studied image, by cutting the image into q sub-images $(I_k)_{k \in \{1,\ldots,q\}}$ with size $(N_k)_{k \in \{1,\ldots,q\}}$. Then, for each sub-image I_k, $\hat{J}_k$ is computed with the criterion described in Sect. 3.1 leading to an evaluation of δ_p: $\hat{\delta}_{p,k} = \dfrac{N_k - \hat{J}_k}{N_k}$. For the studied dataset in Sect. 5, we used four sub-images combined with a small value of by. We could verify that obtained $\hat{\delta}_{p,k}$ have approximately the same values.

9

227   Finally, we take as estimation of δ_p: $\bar{\delta}_p = \frac{1}{q}\sum_{k=1}^{q}\hat{\delta}_{p,k}$ and $\hat{J}$ is chosen as the closest integer

228 to $(1-\bar{\delta}_p) \times N$.

229   Remark: q must be chosen small enough so that the sub-images are large enough to reflect

230 the studied image in terms of patch density. And q is also chosen to obtain an estimation of

231 δ_p in a "reasonable" computation time.

4. Selecting the number of clusters

4.1. Statistical heuristics

234   A first and simple way to properly assess the number of clusters from a dendrogram is to

235 select the numbers of clusters producing the greater jumps in the plot of the cluster criterion

236 values (ie. here the Ward criterion), against the number of clusters. We refer to this strategy

237 as the jump heuristic.

238   An another natural and popular criterion for choosing a relevant number of clusters K in

239 a hierarchy designed with the Ward criterion is to use the value of K corresponding to the

240 maximum value of the Calinski and Harabasz criterion (CHC, [9])

$$\mathrm{CHC}(K) = \frac{\mathrm{Tr}(B_K)}{(K-1)} \Big/ \frac{\mathrm{Tr}(W_K)}{(N-K)},$$

where B_K and W_K are respectively the between-cluster matrix and the within-cluster matrix
of the partition $C_1,\ldots,C_K$. In the present context, we have

$$\mathrm{Tr}(B_K) = \sum_{k=1}^{K}\mu_{C_k}d_{\chi^2}^2(S_{g_{C_k}}, S_g)$$

and

$$\mathrm{Tr}(W_K) = \sum_{k=1}^{K}\sum_{i \in C_k} f_{i.}d_{\chi^2}^2(S_{g_{C_k}}, \mathcal{S}_i)$$

242 where S_g is the gravity center of the N pixels, and for $k = 1,\ldots,K$, $S_{g_{C_k}}$ is the gravity center

243 of cluster C_k.

244   This criterion has been shown to perform well in practical situations (see [20]).

4.2. Particular considerations in the case of spectral images from Ancient materials science

246   Although we listed above several ways to statistically determine the number of clusters to

247 retain, it is however not recommended to choose a unique number of clusters with a formal

248 technique in the case of ancient material studies. Instead, we here prefer to use the following

249 strategy:

- Preselect several number of clusters using the jump heuristic and the CHC.
- Analyze the preselected clusterings with the help of a specialist of the application domain. Having this purpose in mind, it is desirable to provide the specialist with the mean spectra of the preselected clusters, which represent complementary information to those obtained from usual spectral image processing (eg. ROI integration and full spectral decomposition, see Sect. 1) and are, as such, critical to assess the robustness and benefits of the approach.
- Select with this person the clustering(s) to be interpreted.

The present paper exemplifies in the following section this way of assessing ancient material clusterings.

5. Application to a real world dataset

5.1. Data description

The proposed algorithm has been applied to a spectral image dataset collected on a yet undescribed ca. 100-million-year-old new teleost fish from Morocco (Fig. 1, [16]). The information embedded in this dataset is a synchrotron micro-X-ray fluorescence (μXRF) major-to-trace-elemental map, where a full XRF spectrum has been recorded for each pixel, over a 22.5×22.5 mm^2 area using a scan step of 100×100 μm^2 and a 500 ms counting time ($211 \times 241 = 50,851$ pixels in total; Fig. 1b,c). The experiment was performed at the DifFAbs beamline (SOLEIL synchrotron, Gif-sur-Yvette, France) using a 17.2 keV incident beam focused down to a diameter of 10×7 μm^2.

Very interestingly, the distribution of strontium and yttrium Kα lines, which substitute for calcium in calcium phosphates such as bone apatite [16, 14] and whose information depths under hard X-rays reach 200-300 μm in pure apatite with the used geometry, revealed previously indiscernible anatomical features in this peculiar new fish (Fig. 1b, [16]). They particularly unveil the morphology of the first vertebrae (white arrows in Fig. 1b), the neuro-cranium that extends into a sharp supraoccipital at the top of the skull, the metapterygoid, and the hyomandibular that appears dorsally flared. These new information help deciphering the affinities of this new fossil species (in preparation). The other main outcome of this work was that a false color overlay of the distribution of different rare earth elements (REEs; eg. neodymium and yttrium, red and green distributions in Fig. 1b, respectively) discriminates phosphatized muscles (yellow arrows in Fig. 1b and bone [16].

## 5.2. Resulting hierarchical spatial clustering

In the following, the proposed algorithm has been implemented with R [21] on this image of $N = 211 \times 241 = 50,851$ pixels, for which at each pixel i the spectrum $\mathcal{S}_i$ has $P = 1780$ values. The size of the file containing the dataset is 1.7 GB.

For such a dataset, it is too long to compute the criterion H described in Sect. 3 for all $K \in \{N, ..., 1\}$ in order to determine the switching step $\hat{J}$. Hence, as explained in Sect. 3.2, the image has been cut into $q = 4$ sub-images with size 100×115 and $\hat{J}$ has been computed. So δ_p is evaluated from four $(\hat{\delta}_{p,k})_k$ values obtained on the four sub-images with H computed every 5 agglomerative steps ($by = 5$). We obtained: 0.15913, 0.06957, 0.14435 and 0.14478 respectively for top right, bottom right, bottom left and top left sub-images leading to $\bar{\delta}_p \simeq 0.12946$ and consequently $\hat{J} = 44268$. Note that the $(\hat{\delta}_{p,k})_k$ values are close for the three sub-images having a similar type of morphology, whilst the bottom-right sub-image consist mostly of sediment and is more homogeneous than other sub-images.

To select the number of clusters, we plotted the jump heuristic and the CHC against the number of clusters (starting with two clusters) (Fig. 3). These criteria are here to complement the knowledge of the application domain specialist, in the case of the present example a paleontologist (PG). The jump heuristic leads to propose 6 clusters, whilst the CHC leads to propose either 6 or 9 clusters, corresponding to the two local maxima of the curve.

Looking more precisely at the differences between 6 and 9 clusters, it can be seen that only the light green cluster of the 6-cluster solution is modified (Fig. 3c–e). The difference image (Fig. 3e) illustrates how the light green cluster incorporates three smaller clusters: one with 5 black isolated pixels, one green cluster with 50 isolated pixels, and a light-red cluster with 3014 pixels spread out it several patches. If the additional clusters with 5 and 50 isolated pixels seem of little interest, the light-red cluster appears to be interesting, as it highlights areas richer in iron (asterisks in Fig. 1b) that are not clearly obvious in the μXRF elemental maps obtained using ROI integration or spectral decomposition.

From a paleontological point of view, the segmentation offered by the selected clustering (Fig. 4a) does not improve the visualization of hidden anatomical details, but provides new insights into the chemical composition of the different tissues and materials present in the sample through the mean spectra of the clusters (Fig. 4b). While individual elemental distributions show no strong contrast in the incorporation of light REEs between bone and muscles (Fig. 4c), following the distribution of calcium, which they substitute and that originates from a comparable depth (Fig. 4d), the yttrium distribution shows strong enrichment in the bone as compared to the muscles (Fig. 4e). In fact, in the muscles area (yellow arrows in Fig. 1b), rather than following the type of tissue the yttrium distribution largely follows the thickness of

12
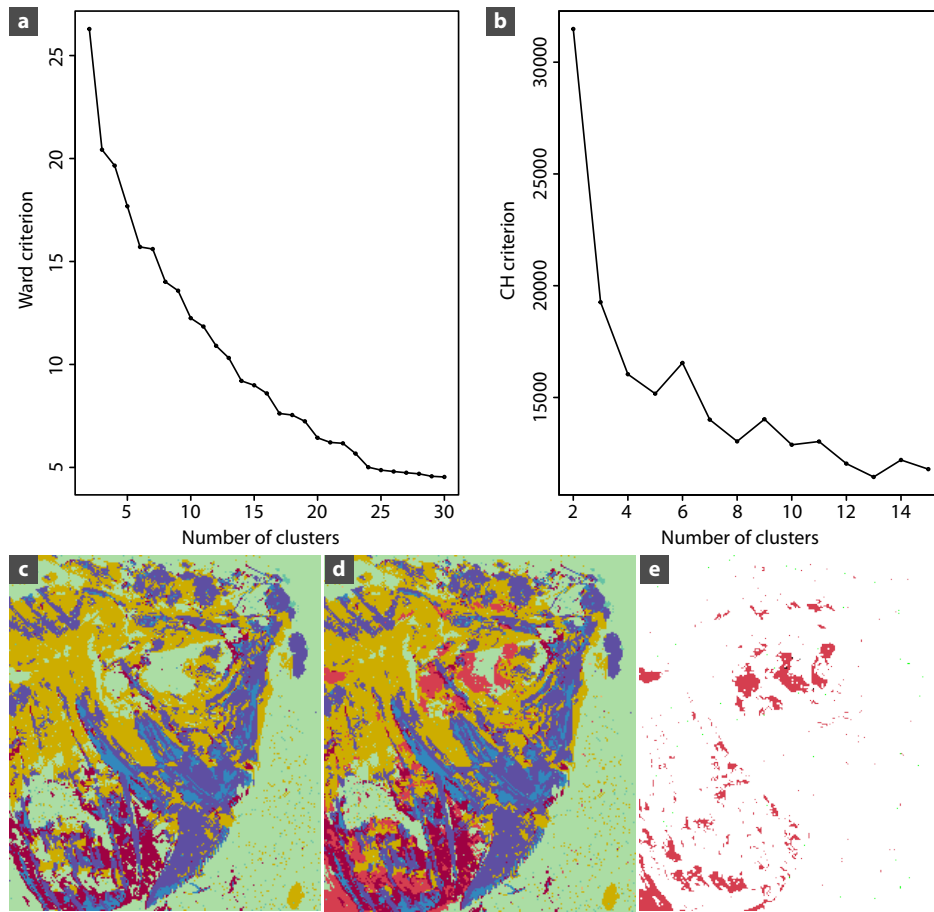
Figure 3. Defining the number of clusters used for hierarchical segmentation.(a, b): Ward (a) and Calinski and Harabasz (b) criteria against the number of clusters (starting with 2 clusters). (c–e): False color distributions obtained for 6 (c) and 9 (d) clusters, and difference (e).

the material as shown by X-ray microtomography where most of the muscles region appear to be very thin or not discernible (Fig. 4f). Consequently, thickness and information depth were likely responsible for the apparent REE contrast. Nevertheless, the selected clustering clearly discriminates bone from phosphatized muscles (blue/purple and dark red clusters in Fig. 4a, respectively) on the basis on the full μXRF spectra. The muscles dark red cluster appears richer in Fe and Pb (Fig. 4b), which come from a reddish fossil biofilm made of iron hydroxides and covering the phosphatized muscles [15, 11, 13] rather than the phosphatic material itself. In turn, the bone blue and purple clusters contain much higher contents in heavier REEs (Lβ1 emission lines from erbium and ytterbium particularly stand out in Fig. 4b, as they do not fall in the same energy domain as major elements [16]). This is most likely again an effect of information depths and thickness of the tissues.

On another hand, the selected clustering isolates well the large, highly absorbing iron grains situated posteriorly to the orbit (asterisks in Fig. 1b; light red cluster in Fig. 4a,b) that prevent segmentation of the first vertebrae and posterior part of the head from the X-ray tomography data (asterisks in Fig. 4f). These grains are particularly rich in Fe, Ti, Cu and Ga, but not so much in Pb (Fig. 4b) and are therefore, besides their larger size, a different material than the reddish thin film of iron hydroxides covering most of the fossil.

By providing a global discrimination of the different materials composing the fossil much faster than a full spectral decomposition (approximatively two hours here for a computer with specifications i5-4590 @ 3.3GHz, 4 Core, four days using the freeware PyMCA [22]), the proposed clustering methodology provides a robust and quick way to extract, "live" at the beamline, chemical information not hampered by local heterogeneity or contamination for further higher resolution mapping of areas of interest, or point analyzes using, e.g., X-ray absorption spectroscopy.
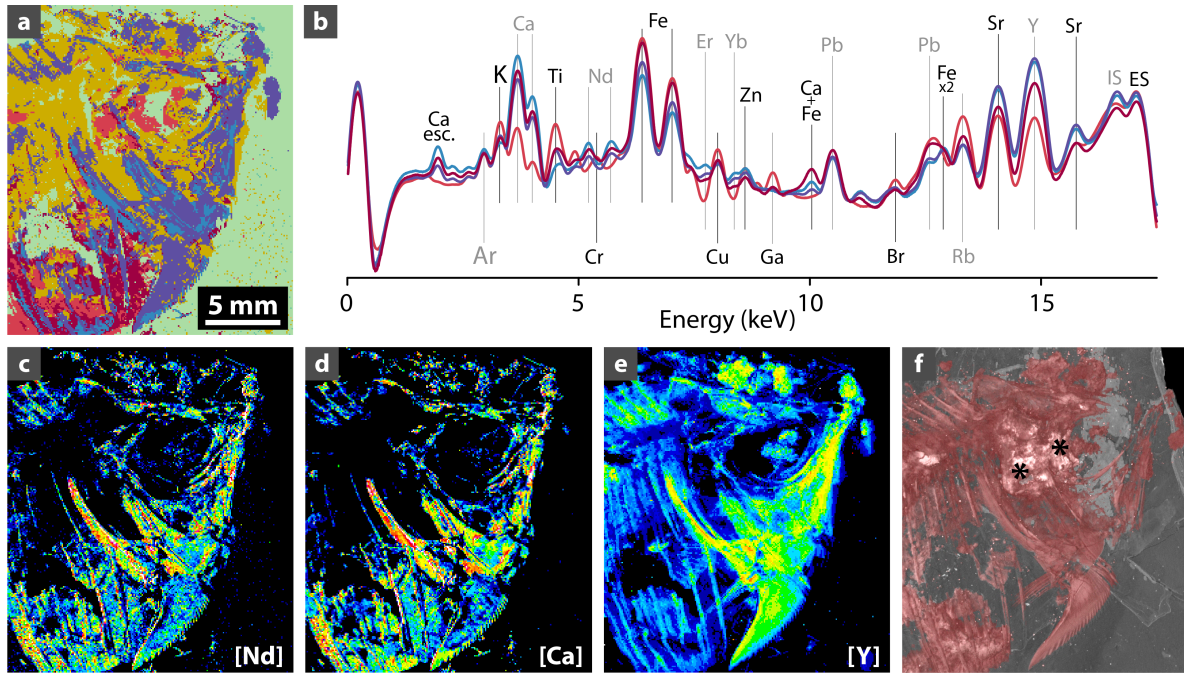
Figure 4. Hierarchical segmentation of the synchrotron μXRF spectral image dataset of the yet undescribed fish (MHNM-KK-OT 03a) from the Jbel Oum Tkout Lagerstätte (Upper Cretaceous, 100 Myr, Morocco). (a): Segmentation results when 9 classes are selected with the proposed algorithm, disabling spatial constraint at agglomerative step $\hat{J} = 44268$. (b): mean spectra from 4 of the 9 classes visible in (a). (c–e): concentration maps of neodymium (c), calcium (d) and yttrium (e). The color scale goes from dark blue (for low concentration) to red (high concentration) going through green and yellow. (f): micro-computed tomography 3D rendering of the fossil within the sedimentary matrix after rapid segmentation. Voxel size: $(24.7 \text{ mm})^3$.

14

5.3. Regarding the chosen switching step J

One may wonder if the value of the switching step, J, has an influence on the results for the choice of the number of clusters and for the clusters shape. In this section we tackle this question by applying the algorithm using switching steps equal to $J = 43000$ and $J = 46000$. In Fig. 5 are the graphic representations of the jump heuristic and the CHC for $J = 43000$ and $J = 46000$, respectively.

For $J = 43000$, the jump heuristic plot leads to propose 6 or 10 clusters while the CHC leads to 3, 10 or 12 clusters (Fig. 5a,b). For $J = 46000$, the jump heuristic plot leads to propose 5 clusters or maybe 9, and the CHC leads to propose 9 clusters (first local maximum) or more (Fig. 5e,f). These results show that the value of the switching step has an influence on the result of the hierarchical clustering. Comparisons of the graphic representations for $J = 43000$, 44268 and 46000 (Fig. 5c,d,g) clearly identify the segmentation resulting from the latter as absolutely unsatisfactory as many fossil areas are found mixed up with the surrounding sediment (Fig. 5g). Graphic representations for $J = 43000$ and 44268 appear in turn very similar. Nevertheless, representation for $J = 44268$ (the computed $\hat{J}$ value, see Sect. 5.2) more accurately reflects elemental distributions (Fig. 1b), particularly regarding the iron-rich phase located around the fish orbit.

6. Assessing robustness of the segmentation to signal to noise ratio

To assess the robustness of the proposed segmentation method in regard of the signal-to-noise ratio (SNR) we prepared simulated data having features close to the one of the experimental dataset used in the previous section, i.e. a spectral image with $N = 211 \times 241 = 50,851$ pixels and at each pixel is associated a spectrum of size $P = 1,700$ canals. Starting with a single realistic model, we generated a family of simulated observation with a decreasing SNR. Performing the segmentation on this family of simulated data, which are all originating from the same generative model, enabled us to assess the effect of SNR levels on the proposed segmentation results. To achieve consistency we generated this simulated dataset in two steps: (i) we constructed a zero noise model that would correspond to a likely observed object; (ii) from this zero noise model we generated simulated observation by applying a noise generation process that mimics the physical observation process while providing control on the noise level of the simulated data. We will present the two steps of this procedure, then the results in terms of segmentation.

6.1. Building a zero noise model and simulating data with controlled SNR

We based our zero noise model on the above studied experimental dataset that we regularized using local polynomial regression smoothing, through the `loess` function in R [21, 10].
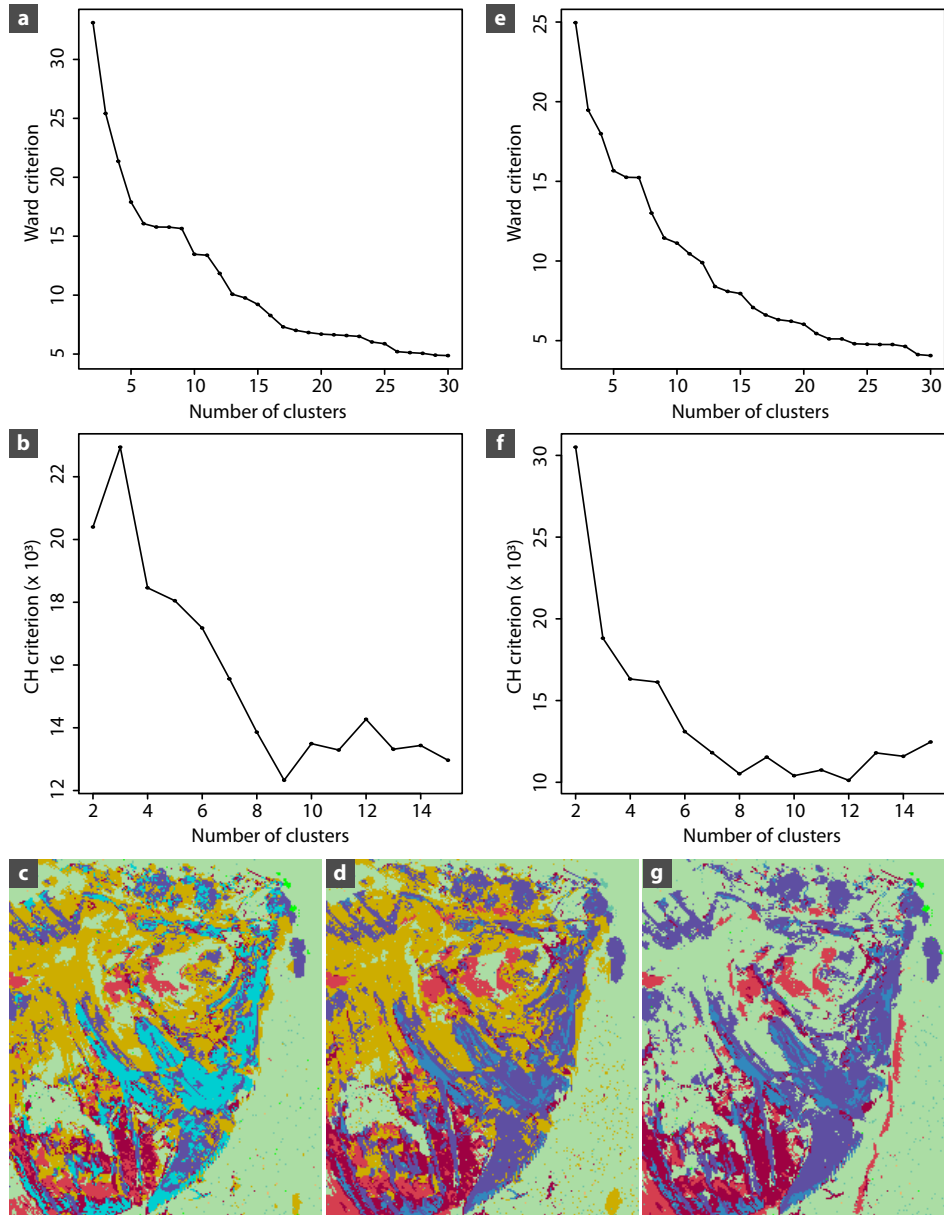
Figure 5. Hierarchical segmentation for different choices of switching step $J = 43000$ and $J = 46000$. (a, b): Ward (a) and Calinski and Harabasz (b) criteria against the number of clusters (starting with 2 clusters) for $J = 43000$. (c): False color distributions obtained for $J = 43000$ (10 clusters). (d): False color distributions obtained for $J = 44268$ (9 clusters). (e, f): Ward (e) and Calinski and Harabasz (f) criteria against the number of clusters (starting with 2 clusters) for $J = 46000$. (g): False color distributions obtained for $J = 46000$ (9 clusters).

To account for the nature and the dynamic of the signal on the observed X-ray fluorescence data, the weight was set to the reciprocal square root $(1/\sqrt{\cdot})$ of the observation when the

16

377 observation is not 0, and to 1 otherwise. The second important parameter was the span of
378 the filter that we set to 0.02 in order to account for the approximate width of the fluorescence
379 bands on such spectra. Finally, a thresholding was performed on the regularized form so that
380 its value is never lower than 0.001.

381 While this procedure is producing a realistic zero noise X-ray fluorescence spectra in each
382 pixel of our image, it has to be noted that this should not be considered as a ground truth
383 version of the observation. Indeed, since each spectrum is dealt with independently from
384 its neighbors, there is no spatial regularization and the estimations performed are far from
385 optimal for detector channels that have measured a low level of photons.

386 The noise present in the observation is mostly due to the counting statistic of each channel
387 of the detector. Hence, we can generate a simulated observed spectra with the same SNR as the
388 raw observation, by simply replacing the value of the zero noise spectra by a single realization
389 of a Poisson random process with its parameter being the zero noise spectra's value. We
390 generated such a dataset, for which we have, by construction, the ground truth and a SNR
391 equal to the one of the raw dataset. This simulated dataset is later on referred as a plus 0db
392 dataset (p0db in short).

393 Starting from the same zero noise model, we also generated simulated observation with
394 lower SNR. Since each theoretical value is replaced by a Poisson realization, dividing the model
395 by a factor of 2 would decrease the SNR by a factor of $\sqrt{2}$, which correspond to removing
396 3db to the SNR. This simulated dataset is later on referred as a minus 3db dataset (m3db in
397 short). Repeating this procedure two more times enabled us to generate a minus 6db dataset
398 (m6db) and finally a minus 9db dataset (m9db).

399 Each of these datasets resembles what could have been measured if the exposure time
400 was divided by two incrementally. In other words, obtaining for the m3db dataset a spatial
401 clustering similar to that obtained for the p0db dataset would lead to the conclusion that the
402 experiment could have been done twice faster without significant loss in term of the explained
403 morphology of the fossil. A shorter exposure time also means a lower radiation dose for the
404 sample and correspondingly lower risk of alteration during and due to the measurements.

405 One has to note that the protocol we use here to smooth the data is not valid as a denoising
406 algorithm since it has some advert effects on the concentration of the trace elements, and in
407 particular the REEs. Still, while the obtained spectra are not properly estimating the ground
408 truth of this particular fossil, they have all the features making them likely to be present in
409 a fossil. Hence, the generated dataset should be considered as the XRF spectral image of a
410 purely phantom fossil, enabling us to test the proposed hierarchical clustering algorithm on
411 totally controlled data.

## 6.2. Impact of noise on hierarchical spatial clustering results

Following the same process as in Sect. 5.2, we use the criterion H to determine the switching step $\hat{J}$. In Fig. 6, we can see that the curve of H has the expected shape for datasets p0db (Fig. 6a) and m3db (Fig. 6c), while the shape begins to change for dataset m6db (Fig. 6e) and is significantly different in m9db (Fig. 6g) (the curve correspond to the top left quadrant sub-image but the same behaviour is observed for the three other sub-images). The values obtained for these dataset are: $\hat{J} = 44063$ for p0db, $\hat{J} = 45871$ for m3db, $\hat{J} = 48988$ for m6db. Such choice is not possible for dataset m9db for the exact reason explained at the end of Sect. 3.1, hence for each of the four sub-image we took the smallest $\hat{J}_k$ on the right (greater than 8000) such that $H(\hat{J}_k) \geq H(J_{\max}) - sd(H)$ (where here $J_{\max}$ and $sd(H)$ are values computed for the associated sub-image I_k). This lead to choose $\hat{J} = 50387$ for m9db. The higher the noise, the higher the $\hat{J}$, getting closer to the total number of pixels N in the image.

According to the plot of the jump heuristic, to the CHC and to clusters appearing to be interesting from a paleontological point of view, the selected number of clusters is 11 for p0db (Fig. 6b), 10 for m3db (Fig. 6d) and 9 for m6db (Fig. 6f). Concerning the m9db dataset, no fossil morphology can be seen when the selected number of clusters is 10 or lower, hence we have decided to represent the 11-cluster segmentation for this dataset (Fig. 6h).

As expected, similarity of the graphic representations as compared to the original and simulated datasets quickly degrades with increasing noise, and most morphological information is lost for dataset with a SNR greater than or equal to 6db from the original data. Increasing further the level of noise leads to totally unexploitable data, with which the morphology of the sample could hardly be observed, as demonstrated on the m9db simulation (Fig. 6h). Note that, in the m3bd representation (Fig. 6d), the pale yellow triangular area that "appears" on the top right of the image and clusters with some of the fossil corresponds to air (there is no sample there, see Fig. 1a); it otherwise clusters with the sediment in the other noise models, which can be explained by the geometry used during the experiment where the beam came from the right of the sample with a 45° angle, leading for pixels in that area to record the X-rays-sediment interaction below the fossil surface.

7. Discussion

In this article we propose a spatially constrained hierarchical clustering method to be applied on spectral images, in particular on energy resolved X-ray fluorescence images. The first aspect of the method is to choose an agglomerative criteria based on a dissimilarity measure that is consistent with the noise model of the measured spectra. Then, the main

18
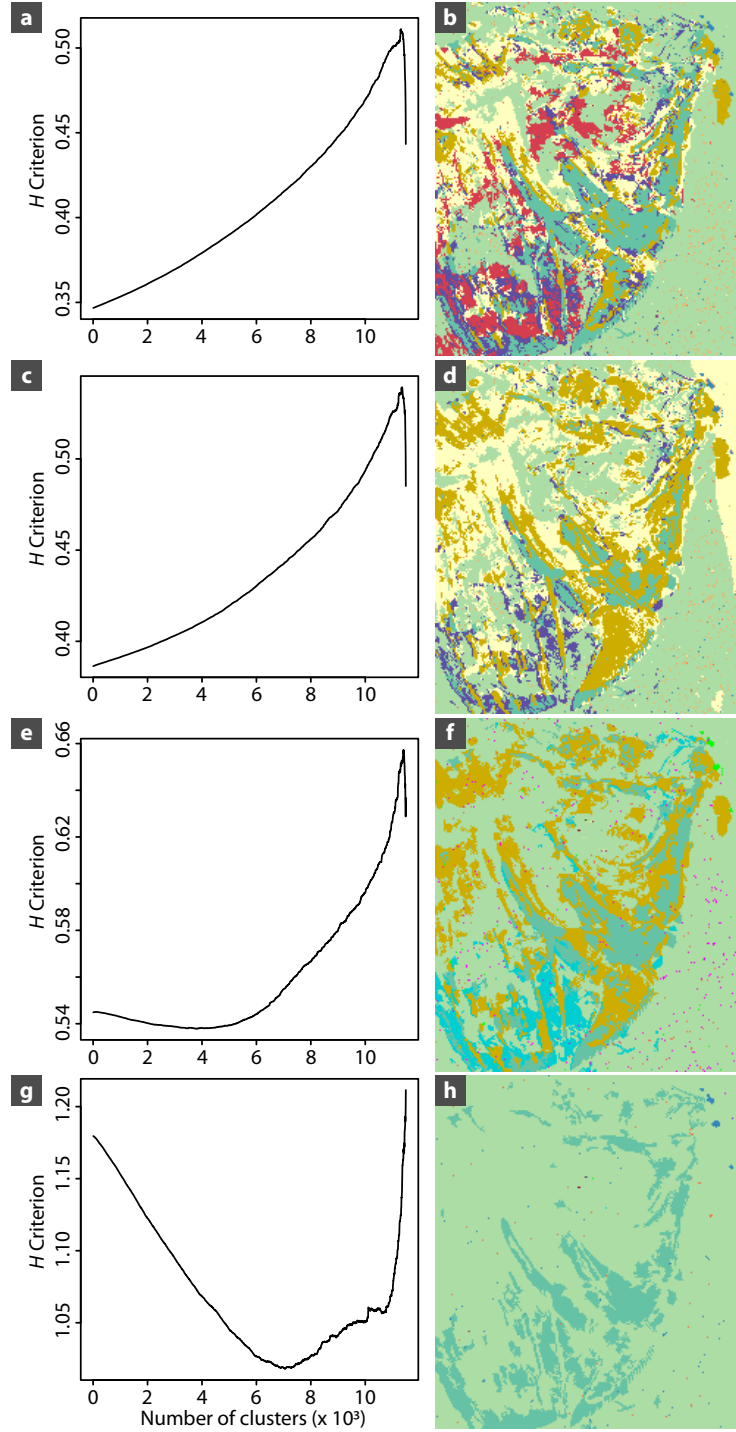
Figure 6. Behavior of the H criterion for selecting the switching step J while adding noise to the zero noise model simulated dataset. The H criterion computed in the top left quadrant sub-image (as explained in Sect. 3.2 and Sect. 5.2) and resulting hierarchical spatial clustering image for the zero noise model (adding 0db) (a,b), and after removing 3db (c,d), 6db (e,f) and 9db (g,h).

aspect of this method is to apply constraints during the agglomerative process such that only spectra belonging to neighboring pixels could be clustered together. While this constraint is meaningful as long as the classes form small clusters on the image, it is obvious that when the number of classes is small this spatial constraint should not be applied anymore, bringing the problem of the proper step at which the spatial constraint should be released. To address this problem, we proposed a heuristic criterion that balances the spatial coherence of the proposed segmentation, as measured through the G penalization, and the between-cluster inertia deriving from the Ward agglomerative criteria. The outcome of this algorithm is a hierarchy of possible segmentations that the practitioner should choose from. To aid this final selection step, the Ward and Calinski and Harabasz criteria are both computed to determine the most significant segmentation within the full hierarchy.

The advantages of such a simple minded algorithm is two-fold: first the general principles of the method do not require deep knowledge of statistical methods and as such can be grasped by the application domain specialist, the paleontologist in the presented example. Second, the computational cost of the segmentation is relatively low, even for a rather large dataset, and the processing time is on par with the typical measurement time for such spectral images, at least few hours. Hence, this method can be applied to the data while the experiment is still ongoing and used for a rapid diagnostic and experimental feedback within the global data acquisition strategy.

As a diagnostic tool, this method helps at finding a balance between a higher signal to noise ratio of individual spectra and the measurement time and radiation dose to which the sample is subjected. In such μXRF imaging modality, the SNR is inversely proportional to the square root of the radiation dose. Increasing the SNR increases the risk of producing radiation-induced damages to the sample during the experiment, but also often leads to increased measurement time and fewer (or smaller) samples being characterized in the allocated time slot. In such a situation it is therefore important to quickly and properly assess the optimal exposure parameters (mostly time, but possibly also beam intensity), which need to be sufficient to produce exploitable spectra while avoiding any risk of radiation-induced damages to the simple and enabling large maps to be collected. Using simulated data, we have shown that the algorithm is robust to an increased level of measurement noise and as such is not only helpful in asserting an optimal measurement time but also in reducing it and lowering the radiation dose.

In our SNR test application, it seems indeed that the behavior of H is a good early indicator of the quality of the observed data, providing insight into the discrimination power of the collected spectra. Indeed the curve in Fig. 6g illustrates a behavior significantly different from

the ones of Fig. 6a,c,e which we link to the fact that the segmentation obtained in Fig. 6h is not very informative. In other words, the behavior of the H criterion as classes get aggregated is a good predictor of the usefulness of the segmentation that will be attained with the data.

Note that while the simulated data tested herein demonstrate that the behavior of the H criterion depends on the SNR, it also depends on the type of morphology of the sample being imaged and in particular in the patch density. This is evidenced in our real data test when comparing the H criterion found in the four quadrants of the image, three of which have a very similar morphology and H criterion curve, while the fourth bottom-right quadrant, with mostly sediment and very little fossil features, produces a slightly different H criterion curve.

As a continuation of the present work, one could assess how the H criterion depends on patch density of the sample. From our currently limited experience, it seems likely that if the studied dataset exhibits a similar type of morphology in all the image, a possibility is to choose a sub-image of size N_0 representative of the image morphology. The parameter δ_p can be then evaluated by $\delta_{p,0} = \frac{N_0 - \hat{J}_0}{N_0}$ (and $\hat{J}$ is chosen as the nearest integer to $(1 - \delta_{p,0}) \times N$), leading to a drastic reduction of the computational cost of the evaluation of this parameter. Furthermore, this promotes δ_p as a scalar descriptor of the image's morphology.

Last but not least, this method provides to the practitioner a complete view of the information contained in a given spectral image dataset. When such data are collected, the prior knowledge on the chemistry of the sample often leads to the selection of very specific features of the spectra to be analyzed. Moreover, although entire μXRF spectra mostly contain XRF elemental information they also include additional, non-elemental signal including escape and sum peaks, as well as inelastic and elastic scattering and peaks from elements present in the air between the sample and the detector such as Ar (Fig. 1c). Depending on the sample, some of these peaks can carry interesting signal and one could need to keep them in the analysis. However, it is often preferred to remove them from the analysis and crop the spectra to the "true" elemental signal only, or only a few peaks, prior to the analysis. This can simply be done at the practitioner's discretion prior to applying the algorithm.

Conversely, we here propose to confront the result of such focused analysis with an analysis based on the full spectra. Indeed, both the focused and complete analysis could be performed using the same algorithm but selecting for each one either a subset or the fullset of the spectral channels of the image. Using such an approach the application scientist could both use the data in a prior knowledge directed approach, verifying pre-existing hypothesis on the nature of the signal to be detected in the spectral image, as well as a unsupervised discovery approach where the full spectral dataset is subjected to the segmentation with a priori on which channel is of importance to exploit the image. Finally, this algorithm might even be

21

used as a post-hoc analysis to test a posteriori the importance of unexpected features of the spectra as discovered discriminant features of the sample, as exemplified herein with the iron-rich phase located around the fossil fish orbit for which the cluster mean spectrum provided complementary and new information to decipher its chemistry.

Contribution of authors.

This work arose from discussions between GC, SXC and AG. SXC proposed the exploitation of spatial constraints and the use of χ^2 as an adapted dissimilarity measure for XRF spectra. GC proposed the heuristic rule to stop applying spatial constraint on the segmentation. AG proposed a version of the χ^2 metric consistent between the spatially constrained initial steps and the unconstrained agglomerative steps, so that Lance and William formulae could be used in this latter part. SXC and AG implemented the algorithm and its result representations in R. SXC proposed and implemented the zero noise model. PG performed all the experimental measurements and interpretations on the fossil, and oriented the algorithm design to ensure results are valuable for the practitioner. All authors contributed to the writing of this manuscript.

Acknowledgments.

Conflict of interest statement.

On behalf of all authors, the corresponding author states that there is no conflict of interest.

BIBLIOGRAPHY

[1] Alfeld, M., Janssens, K.: Strategies for processing mega-pixel x-ray fluorescence hyperspectral data: a case study on a version of Caravaggio's painting Supper at Emmaus. Journal of Analytical Atomic Spectrometry 30(3), 777–789 (2015)

[2] Ambroise, C., Govaert, G.: Convergence of an EM-type algorithm for spatial clustering. Pattern recognition letters 19, 919–327 (1998)

548   [3] Bergamaschi, A., Medjoubi, K., Messaoudi, C., Marco, S., Somogyi, A.: Mmx-i: data-processing software
549   for multimodal x-ray imaging and tomography. Journal of Synchrotron Radiation 23(3), 783–794
550   (2016)

551   [4] Bertrand, L., Cotte, M., Stampanoni, M., Thoury, M., Marone, F., Schöder, S.: Development and trends
552   in synchrotron studies of ancient and historical materials. Physics Reports 519(2), 51–96 (2012).
553   DOI 10.1016/j.physrep.2012.03.003

554   [5] Bertrand, L., Robinet, L., Thoury, M., Janssens, K., Cohen, S.X., Schöder, S.: Cultural heritage and
555   archaeology materials studied by synchrotron spectroscopy and imaging. Applied Physics A, Materials
556   science & processing 106(2), 377–396 (2012). DOI 10.1007/s00339-011-6686-4

557   [6] Bertrand, L., Thoury, M., Anheim, E.: Ancient materials specificities for their synchrotron examination
558   and insights into their epistemological implications. Journal of Cultural Heritage 14(4), 277–289
559   (2013)

560   [7] Bertrand, L., Thoury, M., Gueriau, P., Anheim, É., Cohen, S.: Deciphering the chemistry of cultural
561   heritage: Targeting material properties by coupling spectral imaging with image analysis. Accounts
562   of Chemical Research Online first, 10.1021/acs.accounts.1c00063 (2021)

563   [8] Breiman, L., Friedman, J., Stone, C.J., Olshen, R.A.: Classification and Regression Trees. Taylor &
564   Francis (1984)

565   [9] Calinski, T., Harabasz, A.: A dendrite method for cluster analysis. Communications in Statistics 3, 1–27
566   (1974)

567 [10] Cleveland, W., Grosse, E., Shyu, W.M.: Statistical Models in S, chap. Chapter 8 : Local Regression
568   Models. Wadsworth & Brooks/Cole, New York (1992)

569 [11] Davesne, D., Gueriau, P., Dutheil, D., Bertrand, L.: Exceptional preservation of a cretaceous intestine
570   provides a glimpse of the early ecological diversity of spiny-rayed fishes (acanthomorpha, teleostei).
571   Scientific Reports 8, 8509 (2018)

572 [12] Everitt, B.S., Landau, S., Leese, M., Stahl, D.: Cluster Analysis, 5th edition. Wiley (2010)

573 [13] Gueriau, P., Bernard, S., Farges, F., Mocuta, C., Dutheil, D.B., Adatte, T., Bomou, B., Godet, M.,
574   Thiaudière, D., Charbonnier, S., et al.: Oxidative conditions can lead to exceptional preservation
575   through phosphatization. Geology (2020)

576 [14] Gueriau, P., Jauvion, C., Mocuta, M.: Show me your yttrium, and i will tell you who you are: implications
577   for fossil imaging. Palaeontology 61(6), 981–990 (2018)

578 [15] Gueriau, P., Mocuta, C., Bertrand, L.: Cerium anomaly at microscale in fossils. Analytical Chemistry
579   87(17), 8827–88367 (2015)

580 [16] Gueriau, P., Mocuta C.and Dutheil, D., Cohen, S., Thiaudière, D., the OT1 Consortium, Charbonnier,
581   S., Clément, G., Bertrand, L.: Trace elemental imaging of rare earth elements discriminates tissues
582   at microscale in flat fossils. PLoS One 9(1), e86946 (2014)

583 [17] Gueriau, P., Réguer, S., Leclercq, N., Cupello, C., Brito, P., Jauvion, C., Morel, S., Charbonnier, S., Thi-
584   audière, D., Mocuta, C.: Visualizing mineralization processes and fossil anatomy using synchronous
585   synchrotron X-ray fluorescence and X-ray diffraction mapping. Journal of the Royal Society Interface
586   17(169), 20200216 (2020). DOI 10.1098/rsif.2020.0216

587 [18] Lance, G.N., Williams, W.T.: A general theory of classificatory sorting strategies: II. Clustering systems.
588   The Computer Journal 10(3), 271–277 (1967). DOI 10.1093/comjnl/10.3.271

589 [19] Lebart, L.: Programme d'agrégation avec contrainte. Cahiers de L'analyse des Données 3, 275–287 (1978)

590 [20] Milligan, G., Cooper, M.: An examination of procedures for determining the number of clusters in a data

591   set. Psychometrika 50, 159–179 (1985)

592 [21] R Core Team: R: A Language and Environment for Statistical Computing. R Foundation for Statistical
593   Computing, Vienna, Austria (2020). URL https://www.R-project.org/

594 [22] Solé, V.A., Papillon, E., Cotte, M., Walter, P., Susini, J.: A multiplatform code for the analysis of
595   energy-dispersive x-ray fluorescence spectra. Spectrochimica Acta B 62, 63–68 (2007)

596 [23] Ward, J.H.: Hierarchical grouping to optimize an objective function. Journal of the American Statistical
597   Association 58, 236–244 (1963)